ARTICLE OPEN

Two-dimensional tellurium-based diodes for RF applications

Abdelrahman M. Askar[1✉], Paula Palacios[2✉], Francisco Pasadas[3✉], Mohamed Saeed[2], Mohammad Reza Mohammadzadeh[1], Renato Negra[2] and Michael M. Adachi[1]

The research of two-dimensional (2D) Tellurium (Te) or tellurene is thriving to address current challenges in emerging thin-film electronic and optoelectronic devices. However, the study of 2D-Te-based devices for high-frequency applications is still lacking in the literature. This work presents a comprehensive study of two types of radio frequency (RF) diodes based on 2D-Te flakes and exploits their distinct properties in two RF applications. First, a metal-insulator-semiconductor (MIS) structure is employed as a nonlinear device in a passive RF mixer, where the achieved conversion loss at 2.5 GHz and 5 GHz is as low as 24 dB and 29 dB, respectively. Then, a metal-semiconductor (MS) diode is tested as a zero-bias millimeter-wave power detector and reaches an outstanding linear-in-dB dynamic range over 40 dB, while having voltage responsivities as high as 257 $V \cdot W^{-1}$ at 1 GHz (up to 1 V detected output voltage) and 47 $V \cdot W^{-1}$ at 2.5 GHz (up to 0.26 V detected output voltage). These results show superior performance compared to other 2D material-based devices in a much more mature technological phase. Thus, the authors believe that this work demonstrates the potential of 2D-Te as a promising material for devices in emerging high-frequency electronics.

npj 2D Materials and Applications (2023)7:70 ; https://doi.org/10.1038/s41699-023-00433-w

INTRODUCTION

Thin-film materials have been investigated for over 30 years, however, 2D electronics became a reality after the exfoliation of graphene in 2004[1]. This material presented unique conducting properties that revolutionized the research field and gave room for a completely new range of flexible, wearable, and transparent devices and circuits[2]. Nevertheless, despite the milestone graphene meant, it intrinsically presents a band structure that hinders its application to some devices, in particular, the performance of graphene-alone field-effect transistors (FETs) is truncated by such physics of the material[2], while it has shown great performance when utilised in diodes[3]. Therefore, by taking advantage of the progress that graphene had led to, the research community has carried on in the investigation of new 2D materials that might overcome the technological challenges graphene has brought to light[4], such as transition-metal dichalcogenide (TMD) materials. Contrary to graphene and Black Phosphorus (BP), TMDs possess the needed bandgap to achieve high ON/OFF ratios and current saturation and are stable at room temperature, although they present lower mobilities. These properties have made them potential candidates to become the next generation of thin-film devices. However, while MoS_2-based *n*-type transistors show excellent performance, the *p*-type counterpart, typically made with WSe_2 or WS_2, still lacks of a comparable performance[5]. This has led once again to the investigation of additional materials that can improve the performance of natural *p*-type TMDs. To the latter group belongs Tellurium or in its 2D form: Tellurene.

Tellurium is environmentally stable and possesses high charge carrier mobility and a sizeable non-zero bandgap, which holds great potential for being disruptive in the field of electronics and optoelectronics in the near future[6]. It was not until 2017 when 2D Tellurium (Tellurene) was first grown by the use of a hydrothermal growth technique, just after being theoretically predicted earlier that same year[7,8]. Then, in 2019, thin films of Tellurium were deposited by using large-scale evaporation[9], and in 2020, large-scale single-crystal arrays were successfully grown by low-temperature crystallization[10]. Ever since, research efforts have been intensified to explore this 2D material to better understand its physical, electrical, optical, thermoelectrical, and quantum properties. Yet, while the vast majority of the literature explores its possibilities in the optical domain[11], its application to electronic devices and circuits is in its infancy. The first 2D Te-based FETs resulted quite promising by showing ON/OFF ratios in the order of 10^6, and field-effect mobilities of about 700 $cm^2 \cdot V^{-1} \cdot s^{-1}$[12]. Furthermore, and more importantly, their air-stable performance at room temperature was demonstrated to last over two months[12]. However, to the best knowledge of the authors, the radio frequency (RF) performance of any Tellurium-based device has not been reported yet. In this work, the RF performance of semiconducting two-dimensional (2D) Te-based diodes is demonstrated by two different structures: a metal-insulator-semiconductor (MIS) diode and a metal-semiconductor (MS) diode. The paper is structured such that first, the devices are introduced by presenting their structure and fabrication methods. Then, the electrostatics and charge transfer mechanisms are studied followed by their full characterization both in DC and RF domains. This analysis is fundamental to evaluate the impact of the bias-tunable Schottky barrier height on the electrical performance of Te-based diodes. To continue, each device is integrated into a circuit in order to validate its potential for RF nonlinear applications. Finally, the results are discussed and the comparison with the state-of-the-art is presented.

RESULTS

2D Te-based diodes

The fabricated metal-insulator-semiconductor device is illustrated in Fig. 1a. The structure consists of (from bottom to top) a Ti metal contact (cathode), a TiO_2 insulating layer, a 2D Te flake that was prepared following a standard hydrothermal synthesis procedure,

[1]School of Engineering Science, Simon Fraser University, 8888 University Drive, Burnaby, British Columbia V5A 1S6, Canada. [2]Chair of High Frequency Electronics (HFE), RWTH Aachen University, Koppernikusstr. 16, 52074 Aachen, Germany. [3]Pervasive Electronics Advanced Research Laboratory (PEARL), Departamento de Electrónica y Tecnología de Computadores, Universidad de Granada, Campus de Fuentenueva, 18071 Granada, Spain. ✉email: aaskar@sfu.ca; paula.palacios@hfe.rwth-aachen.de; fpasadas@ugr.es

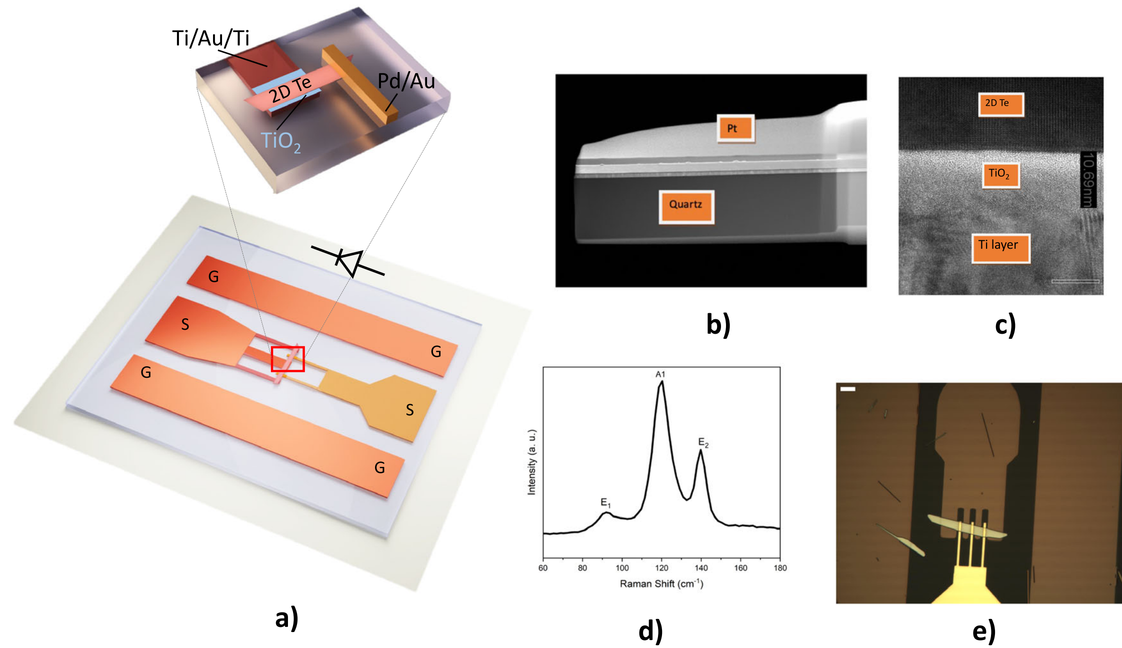

Fig. 1 MIS structure analysis of the TIM diode. a Schematic diode cross-section and layout with GSG pads to enable RF characterization. **b** Low-resolution STEM-HAADF cross-section image of the lift-out sample at low magnification, which shows the main layers of the device along with a Pt protection layer. **c** High-resolution TEM image of the core of the device, the interface of the 2D Te, the TiO_2, and the Ti layer are shown. Scale: 10 nm (**d**) Raman spectra for a 2D Te flake drop casted on a SiO_2/Si substrate. The three main characteristic peaks, as previously reported in[12], can be observed. **e** Microphotograph of the device-under-test TIM diode. Scale:13.86 nm.

as reported in[12] (see Methods), and a Pd electrode (anode). Since Tellurium is naturally a *p*-type semiconductor, in an anode-to-cathode order, the configured heterostructure forms the Tellurium-Insulator-Metal (TIM) diode. Thus, in the following, both terms TIM diode and MIS structure are interchangeably used. In its fabrication, the bottom Ti contact is embedded into a quartz substrate using a standard lithography process and wet etching. This is followed by the deposition of a Ti/Au/Ti (10 nm/170 nm/10 nm) metal stack. The TiO_2 is then deposited by RF plasma sputtering (with a nominal thickness of 8 nm) using the same pattern as for the metal deposition. Then, a lift-off process is carried out to complete the bottom contact and the insulating layer of the device. To continue, the 2D Te flake is deterministically transferred to the pre-patterned bottom contacts[13]. Finally, the Pd/Au contacts are patterned using optical lithography and deposited using e-beam evaporation to form an ohmic contact with the 2D Te and finalize the device fabrication. As indicated in Fig. 1a, the layout of this device presents an interdigitated structure in order to scale the active area (contact between the Te and the oxide) not only by the size of the flake but also by the number of fingers. Additionally, the top (Pd/Au) metal includes a typical ground-signal-ground (GSG) structure to allow both DC and RF characterization. It should be noted that, in this work, quartz is chosen as a substrate because it is non-conductive, which leads to a reduction in resistive losses (crucial in RF circuits) and had been previously verified in graphene-based diodes[2]. Nevertheless, as with other 2D material-based devices, the used processes in the fabrication can, in principle, be translated to other substrates and quartz can be replaced, for instance, by a flexible substrate. Further empirical analysis would be needed to determine the difference in performance.

A High-Resolution TEM (HRTEM) image of the cross-section of the fabricated device, and the Raman spectroscopy are shown in Fig. 1c and Fig. 1d, respectively. The 2D Te can be easily distinguished in the HRTEM image through its highly ordered structure and the abrupt interface, then the TiO_2 is discerned, with its amorphous nature along with its smooth transition to the Ti layer, which appears to be polycrystalline. The TiO_2 grows naturally on the Ti contact once exposed to the atmospheric environment (around 2 nm-thick layer), the remaining thickness of the TiO_2 layer was deposited by TiO_2 sputtering, as already discussed, forming a barrier with a total thickness of around 10 nm. Further analysis of the deposited layers can be found in Supplementary Fig. 1-Supplementary Fig. 4. Finally, the micro-photograph of the device-under-test is shown in Fig. 1e.

The second diode sample consists of an MS heterostructure that, analogously to the previous one, forms the Tellurium-metal (TM) diode, as shown in Fig. 2a. The device is fabricated by transferring 2D Te flakes to the quartz substrate. Next, the first contact (Ti/Au) (10 nm/170 nm) is patterned and deposited using optical lithography, e-beam evaporation, and lift-off process. Then, the Pd/Au contact (10 nm/170 nm) is similarly patterned, deposited, and a lift-off process follows which completes the fabrication of the MS device. However, the fabricated TM diode, shown in Fig. 2b, has been simplified compared to the previously TIM design, shown in Fig. 1e, in terms of the finger arrangement. Despite the use of the interdigitated structures in bulk semiconductor diodes and other 2D graphene-based devices[2,14], the TIM diode (fabricated first) demonstrated that this approach cannot be fully exploited with 2D-Te based on flakes, where the control of the width is more important. Furthermore, as it is later observed in the RF modelling, the thin fingers are responsible of a higher series impedance at higher frequencies. Thus, without a critical impact in the performance of the proof-of-concept devices, the TM devices were implemented without fingers.

The band diagram of the MIS heterostructure is shown in Fig. 3a. Due to the charge transfer between the anode metal and the Te-channel, the formation of a dipole (gap) layer with an equilibrium separation distance between the metal and the semiconductor of t_{dip} is considered[15]. The anode metal and the low-dimensional channel are assumed in equilibrium; hence, the Fermi energies are aligned. By the application of the charge neutrality at the Te-channel interfaces in Fig. 3a, the electrostatics

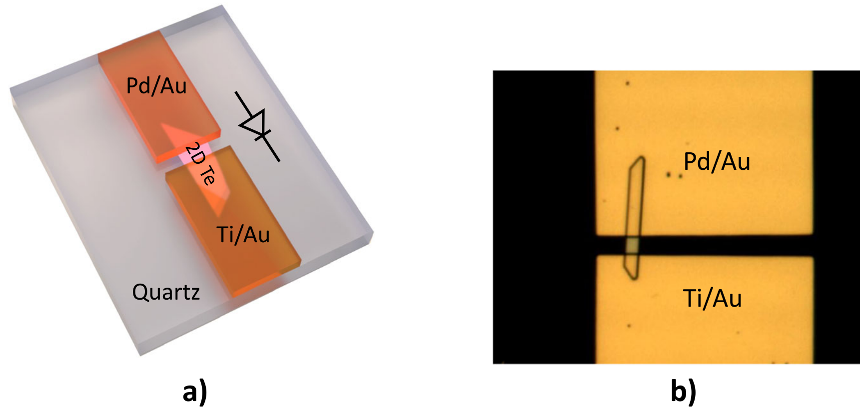

Fig. 2 Tellurium-metal diode. a Schematic illustration of the MS heterostructure and (**b**) top-down view microscope image of the TM diode.

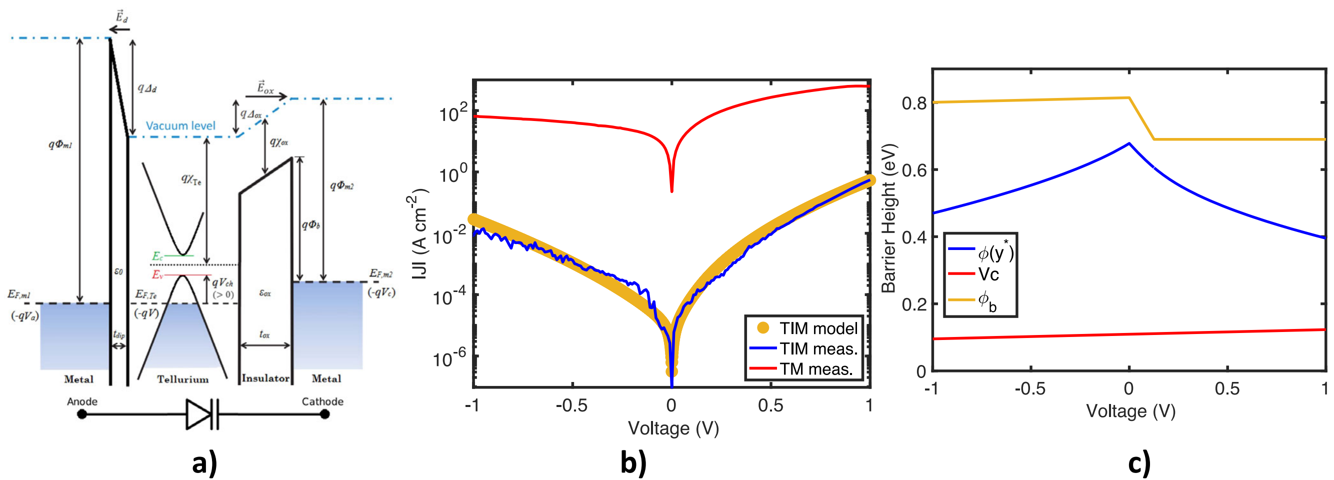

Fig. 3 Characteristics curves of the 2D Te-based diodes. a Band diagram of a metal-Tellurium-insulator-metal heterostructure. q is the elementary charge; ϕ_{m1} (ϕ_{m2}) is the anode (cathode) metal work function; χ_{ox} (χ_{Te}) is the electron affinity of the insulator (intrinsic Te-channel); $E_{F,m1} = -qV_a$, $E_{F,m2} = -qV_c$, and $E_{F,Te} = -qV$ are the Fermi energy levels in both metals and Te-channel, respectively, with V_a (V_c) being the applied anode (cathode) voltage and $V_{bias} = V_a - V_c$. The conduction (valence) band edge in the Te-channel is E_c (E_v), with an energy band gap of $E_{g,Te} = E_c - E_v$. The channel potential for p-type (n-type) Tellurium is $V_{ch} = (E_v - E_F)/q$ ($V_{ch} = (E_c - E_F)/q$). $\vec{E}_{ox}$ ($\vec{E}_d$) is the electric field within the oxide (dipole layer); ϵ_{ox} (ϵ_0) is the oxide (vacuum) permittivity; and t_{ox} (t_{dip}) is the oxide thickness (equilibrium dipole separation distance). **b** Current densities of the TIM diode with sputtered oxide and the TM diode (solid lines) together with the model results for the TIM diode (scatter). The total active areas are estimated from an HRTEM photograph to 323 μm^2 for the TIM and 16 μm^2 for the TM. **c** Bias-dependence of the chemical potential (red) in the Te-channel and the barrier height considering (blue) and without (yellow) accounting for the Schottky barrier lowering due to the image force effect.

of the TIM diode can be derived as follows:

$$\begin{aligned} \phi_{Pd} &= \Delta_d + \chi_{Te} \mp \tfrac{E_{g,Te}}{2q} - V_{ch} \\ \phi_{Ti} &= -\Delta_{ox} + \chi_{Te} \mp \tfrac{E_{g,Te}}{2q} - V_{ch} - V_{bias} \\ & Q_{m1} + Q_{m2} + Q_{Te} = 0 \end{aligned} \tag{1}$$

where Δ_d (Δ_{ox}) is the potential drop across the dipole layer (oxide barrier) due to the charge transfer; the potentials V_{bias}, ϕ_{Ti} (ϕ_{Pd}), χ_{Te}, and $E_{g,Te}/q$ are the applied anode-cathode bias, the Ti-(Pd-) work-function, and the intrinsic Te-electron affinity and the potential of the bandgap, respectively, with q being the elementary charge; and $Q_{m1} = -C_{dip}\Delta_d$ ($Q_{m2} = C_{ox}\Delta_{ox}$) is the charge density induced in the anode (cathode) metal. The capacitive coupling originated at the considered dipole layer reads $C_{dip} = \epsilon_0/t_{dip}$ and the geometric oxide capacitance per unit area is $C_{ox} = \epsilon_{ox}\epsilon_0/t_{ox}$, where ϵ_0 is the vacuum permittivity, ϵ_{ox} is the relative permittivity of the TiO_2 barrier and t_{ox} is the oxide thickness. The Te-channel charge density is $Q_{Te} = Q_{net}(V_{ch}) + Q_{res}$, where Q_{res} is the residual charge per unit area in the channel; and $Q_{net}(V_{ch})$ is the overall net charge density in the Te-channel and is calculated by assuming the effective mass approximation, i. e., a parabolic dispersion relationship at the highest (lowest) energies of the valence (conduction) band; and using *Fermi-Dirac* statistics as follows:

$$\begin{aligned} Q_{net}(V_{ch}) &= q[p(V_{ch}) - n(V_{ch})] \\ &= qV_t \begin{cases} C_{dq,p}\log\left(1 + e^{\frac{V_{ch}}{V_t}}\right) - C_{dq,n}\log\left(1 + e^{-\frac{V_{ch} + \frac{E_{g,Te}}{q}}{V_t}}\right) & \text{if } p-\text{type} \\ C_{dq,p}\log\left(1 + e^{\frac{V_{ch} - \frac{E_{g,Te}}{q}}{V_t}}\right) - C_{dq,n}\log\left(1 + e^{\frac{-V_{ch}}{V_t}}\right) & \text{if } n-\text{type} \end{cases} \end{aligned} \tag{2}$$

where $V_t = k_BT/q$ is the thermal voltage, k_B is the Boltzmann constant, T is the temperature; and $C_{dq,n} = q^2D_{0,n}$ ($C_{dq,p} = q^2D_{0,p}$) is defined as the electron (hole) degenerated-quantum capacitance, that corresponds to the upper-limit achievable when the electron (hole) density becomes heavily degenerated[16]. $D_{0,n} = g_{e,1}(m^*_{e,1}/2\pi\hbar^2) + g_{e,2}(m^*_{e,2}/2\pi\hbar^2)\exp[-\Delta E_{e,1\to 2}/k_BT]$ $(D_{0,p} = g_{h,1}$

$(m^*_{h,1}/2\pi\hbar^2) + g_{h,2}(m^*_{h,2}/2\pi\hbar^2)\exp[-\Delta E_{h,1\to2}/k_BT])$ is the density of states in the conduction (valence) band, with $\hbar$ standing for the reduced Planck's constant, $g_{e,1}$, $g_{e,2}$ ($g_{h,1}$, $g_{h,2}$) are the degeneracy factors, and $m^*_{e,1}$, $m^*_{e,2}$ ($m^*_{h,1}$, $m^*_{h,2}$) are the conduction (valence) band effective masses at the first and second valleys, respectively, in the vicinity of the H-point in the case of Tellurium[17,18]. The second conduction (valence) valley could be non-negligible as occurs in most TMDs since the energy separation between the lowest conduction (highest valence) valleys, $\Delta E_{e,1\to2}$ ($\Delta E_{h,1\to2}$) is only around $2k_BT$[19,20]. Thus, two conduction (valence) band valleys may participate in the transport process. The rest of the valleys are considered, on the contrary, far away in energy to contribute to the electrical conduction and, hence, can be neglected for practical purposes. Additionally, the chemical potential, V_{ch}, represents the shift of the quasi-Fermi level with respect to the conduction (valence) band edge, therefore, the negative (positive) sign in equation (1) applies when the overall Q_{net} in the channel is negative (positive), *i.e.*, the channel is *n*-type (*p*-type). Only a quasi-Fermi level has been considered for both kinds of carriers, namely the parallel connection of independent *n*-type and *p*-type channels is assumed to keep the model compact and thus compatible with circuit simulators. These assumptions physically mean that the carrier generation-recombination processes in the low-dimensional Te-channel are fast enough to establish equilibrium between both types of carriers. In this regard, V_{ch} specifically reads:

$$V_{ch} = \begin{cases} (E_v - E_F)/q & \text{if } Q_{net}<0 \equiv p-\text{type} \\ (E_c - E_F)/q & \text{if } Q_{net}<0 \equiv n-\text{type}. \end{cases} \quad (3)$$

Combining the equations in (1), the electrostatics of the TIM heterostructure can be described by the following expression:

$$(C_{ox} + C_{dip})V_{ch} - C_{ox}V_{bias} + Q_{net}(V_{ch}) = Q_0, \quad (4)$$

where $Q_0 = C_{ox}\phi_{Ti} + C_{dip}\phi_{Pd} - (C_{ox} + C_{dip})(\chi_{Te} \mp E_{g,Te}/2q) - Q_{res}$ and the negative (positive) sign applies when the channel is *n*-type (*p*-type).

The out-of-plane transport through the TIM diode is considered to be the vertical emission of carriers from/to the Te-channel plane to/from the bulk Ti-metal through the insulator barrier[21]. Under a reasonable practical vertical electric field (namely considering a bias window $V_{bias} \in [-1, 1]$ V), the static current flow can be attributed to the thermionic emission of carriers above the barrier. While the in-plane electron transport properties of 2D materials have been extensively studied along the time[22], the out-of-plane transport, such as the electron vertical emission from the plane, has been recently reviewed in[23] for heterostructures based on low-dimensional materials so that accounting the possible difference in the dimensionality between the channel and the metal [24].

Regarding the TM device, the carrier transport is expected to be dominated by a combination of field emission and thermionic field emission given the large currents that can flow even at low applied biases as observed in Fig. 3b. In metal-semiconductor contacts, the general theory of field emission and thermionic field emission must be carefully addressed[25–27], especially an analysis of the surface states in Tellurium is needed to properly address the transport in this heterostructure. Nevertheless, the TIM current density can be predicted as follows[24]:

$$J_{th} = q\frac{C_{dq}V_t^2}{2\pi\hbar}e^{-\frac{\phi_b - \frac{\delta_p^2}{2V_t}}{V_t}}\left(e^{\frac{V_{bias}}{\eta V_t}} - 1\right), \quad (5)$$

where ϕ_b is the Schottky barrier height (SBH) (see Fig. 3c); δ_p estimates the spreading of the Fermi level; η is the ideality factor; and $C_{dq} = \sqrt{C_{dq,n}C_{dq,p}}$. Note that a scaling of T^2 ($V_t^2 = k_B^2T^2/q^2$) is also predicted for low-dimensional materials with a parabolic dispersion relationship, in agreement with the Richardson-Dushman scaling for bulk materials[23,24].

Additionally, the image force (IF) effect is included by accounting of the possible Schottky barrier lowering[28,29]. In this regard, the position-dependence of the SBH that includes the image potential along the insulator thickness (*y*-coordinate) is given by:

$$\phi(y) = \phi_b - \Delta_{ox}\frac{y}{t_{ox}} - 1.15\frac{\log 2}{8\pi}\frac{q}{C_{ox}}\frac{1}{y(y - t_{ox})} \quad (6)$$

where the Schottky barrier lowering (SBL) produced by the IF effect is basically

$$SBL = \Delta_{ox}\frac{y^*}{t_{ox}} + 1.15\frac{\log 2}{8\pi}\frac{q}{C_{ox}}\frac{1}{y^*(y^* - t_{ox})}. \quad (7)$$

The highest $\phi(y^*)$ that defines the insulator barrier height is found requiring $d\phi(y^*)/dy = 0$, hence, $\phi(y^*)$ will replace ϕ_b in (5) to include the lowering of the barrier due to the IF effects[30].

The devices are characterized at DC, following the procedure detailed in the Methods section. In Fig. 3b, the measured (solid lines) current density for the MIS and MS devices are shown, respectively, together with the theoretical results (symbols) from the above-mentioned model for the TIM structure, with the parameters collected in Table 1, showing an excellent agreement. Figure 3c shows the bias-dependence of the (red) chemical potential in the Te-channel and the barrier height considering (blue) and without accounting for (yellow) the SBL due to the image force effect. Regarding Fig. 3a, we can observe the considerable current increase in the case of the TM device, bringing to light the impact of a considerable reduction of the barrier. Indeed, Supplementary Fig. 5 depicts sketches of the band diagrams of general MIS and MS structures (for $\phi_s > \phi_m$), where the barrier height can be compared, *i.e.*, the MIS barrier height is $q\phi_{b,MIS} = q\phi_s - q\chi_{ox}$, while the MS barrier height is $q\phi_{b,MS} = E_{g,s} + q\chi_s - q\phi_m$. Besides, Supplementary Fig. 6 and Supplementary Fig. 7 collect further DC characterizations of the TIM and TM heterostructures, respectively. From V_{ch} in Fig. 3c (red), we can observe that the Te-channel is *p*-type within the bias window considered. Additionally, the barrier height without the SBL (yellow) is tunable for biases $V_{bias} < 0.126$ V due to the work-function tunability of the Te-channel, which is $\chi_{Te} \mp \frac{E_{g,Te}}{2q} - V_{ch}$, according to Fig. 3a. For biases $V_{bias} > 0.126$ V, the $\vec{E}_{ox}$ within the TiO_2 barrier change of sign (c.f. Fig. 3a), so that the barrier height, ϕ_b, (without accounting the SBL due to IF effects) is fixed at $\phi_{Ti} - \chi_{TiO_2}$. However, the barrier, $\phi(y^*)$, is tunable due to the SBL by including the effect of image force (blue), which is critical in the TIM structure as previously reported by some of the authors in[30] for metal-insulator-graphene (MIG) devices, given that TIM and MIG devices are based on a similar TiO_2 barrier. Additionally, we can estimate the junction capacitance equal to 1.7 pF by $C_j = dQ_{net}/dV_{bias}$, which presents small bias-dependence (not shown) because the Te-channel degenerated in the TIM technology collected in Table 1 within the considered bias window.

Table 1. TIM model parameters.

$W \times L$	(μm^2)	324	$g_{e,1}$	4[54–56]
C_{ox}	($\mu F \cdot cm^{-2}$)	0.52[30]	$g_{e,2}$	0[54–56]
C_{dip}	($\mu F \cdot cm^{-2}$)	4.22[15]	$g_{h,1}$	2[54–56]
ϕ_{Ti}	(eV)	4.66[15]	$g_{h,2}$	2[54–56]
ϕ_{Pd}	(eV)	5.67[15]	$m^*_{e,1}/m_0$	0.085[57–59]
χ_{Te}	(eV)	4.5[60]	$m^*_{e,2}/m_0$	0[54–56]
$E_{g,Te}$	(eV)	0.35[17,54–56,59]	$m^*_{h,1}/m_0$	0.5[59,61,62]
χ_{TiO_2}	(eV)	4	$m^*_{h,2}/m_0$	0.1[17,59]
Q_{res}	($C \cdot cm^{-2}$)	0	$\Delta E_{e,1\to2}$ (eV)	0[54–56]
T	(K)	295	$\Delta E_{h,1\to2}$ (eV)	0.15[55,56]

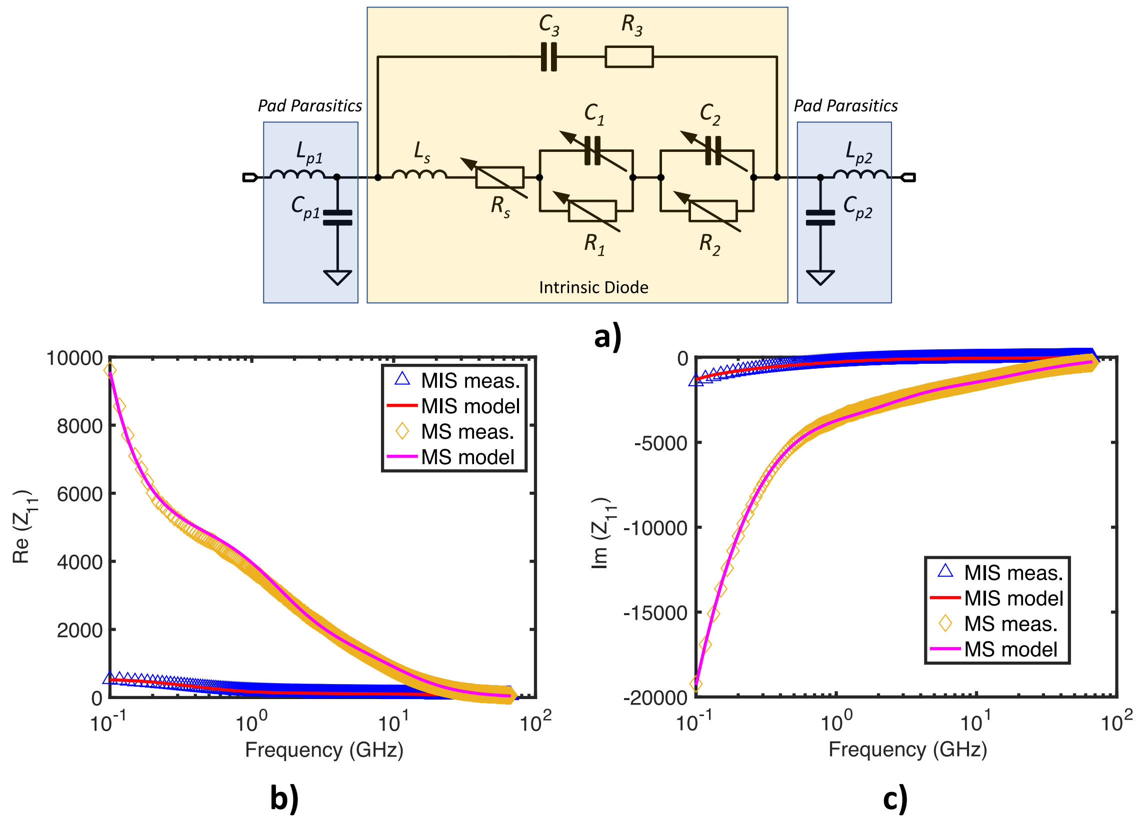

Fig. 4 RF small-signal characterization of Te-based diodes. a Equivalent circuit extracted from the S-parameter measurements. The (**b**) real and (**c**) imaginary parts of the input impedance of the diode over frequency verify the good agreement between measurements and the equivalent circuit.

Table 2. Extracted parameters from the *S*-parameter measurements.

	C_1 (pF)	R_1 (MΩ)	C_2 (pF)	R_2 (Ω)	C_3 (pF)	R_3 (Ω)	R_s (Ω)	L_s (nH)	C_{p1} (fF)	L_{p1} (pH)	C_{p2} (fF)	L_{p2} (pH)
MIS (10 nm) @-1.5 V	1.3	1	0.9	450	0.045	145	140	0.07	1.5	55	3	1
MS @0 V	0.073	0.082	0.028	2900	0.0027	–	3000	–	4	200	4	200

From the DC performance, three rectifying figures-of-merit (FOMs) can be evaluated to estimate the suitability of nonlinear devices to perform as detectors and rectifiers. These FOMs[31,32] are the asymmetry, nonlinearity and responsivity. Firstly, the asymmetry ($f_{ASYM} = |J_{forward}/J_{reverse}|$) is an indicator of the presence of rectification, where $f_{ASYM} = 1$ means that no rectification occurs and the higher the slope in the asymmetry-bias curve, the higher rectification. Then, the nonlinearity ($f_{NL} = (dJ/dV)/(J/V)$) is a measure of the deviation from a resistor-like behavior. Therefore, a large parasitic series resistance causes low nonlinearity. Finally, the responsivity ($f_{RES} = (d^2J/d^2V)/(2 \cdot (dJ/dV))$), is a measure of the DC current sensitivity to input power. The extracted FOMs are included in Supplementary Fig. 6 and Supplementary Fig. 7 for both types of diode. Thus, in agreement with the already reported literature[33], the impact of the thickness of the oxide in the TIM diodes is reflected in the asymmetry of the devices. From Fig. 3a and the extracted FOMs it is observed that the asymmetry decreases when the oxide layer is removed. Furthermore, the current density is considerably higher in the MS diode along the whole bias window considered, i. e., at 1 V it is around three orders of magnitude higher, while five orders of magnitude higher at 0 V. These values indicate the promising performance of TIM diodes as switches and for biased applications while showing the high potential of the TM diode for zero-biased applications due to its strong nonlinear behavior around the zero-bias condition. Whereas the obtained DC FOMs are a good indicator of the expected performance, the performance over frequency must be addressed by analyzing the RF measurements.

The extracted equivalent circuit for both the TIM and the TM diode is depicted in Fig. 4a. The parameter values were extracted from the measured *S*-parameters, as indicated in Methods, and are detailed in Table 2 for both diode variants. The obtained results demonstrate the excellent agreement with the RF measurements for a frequency band ranging from 10 MHz to 67 GHz, as shown in Fig. 4a, c, and Supplementary Fig. 8. Contrarily to widely reported Schottky diodes[32], it is observed that the small-signal equivalent circuit presents a more complex structure than only the series combination of a parasitic resistance (R_s) with the parallel pair formed by a junction capacitance (C_j) and a junction resistance (R_j). In the Te-based devices, the parallel combination of the capacitance, C_1, and resistance, R_1, is analogous to the just mentioned R_j and C_j. Thus, the good agreement between the aforementioned predicted junction capacitance in the theoretical model (1.7 pF) and the value needed for fitting the equivalent circuit (1.3 pF) should be noted. It is precisely due to the higher value of the capacitor compared to the rest, that this first block plays a bigger role at lower frequencies. On the other hand, the parallel combination of C_2 and R_2 impacts the performance at

medium and high frequencies. Similar equivalent circuits that include these first two blocks had been previously reported for other MIS structures[34,35], PIN diodes[36] and even in metal-insulator-graphene (MIG) diodes[37]. The explanation that these other works have provided for this distinct behavior that leads to further *RC* pairs is either the irregular density of surface states in the insulator layer in the former two or the quantum capacitance in the latter. In our work, since both the TIM and TM diodes present both pairs, these elements might reflect the Te-channel areas that are not under the electrostatic control of the Ti-electrode and/or the possible formation of a charged dipole in the Te flake. Yet, further analysis would need to be pursued to associate these elements with the heterostructure. Next, the series combination of L_s and R_s models the behavior of the Pd-Te contact. Importantly, L_s is found to be negligible in the TM diode, probably because it lacks long thin fingers. Finally, R_3 and C_3, only found in the TIM diode, could be associated with the small thickness of the oxide in such MIS devices according to the work in[38].

The impact of the small-signal behavior of the diodes on the potential applications is crucial. From Fig. 4a it can be observed that both in-series *RC* blocks vary with the applied bias voltage and so is the series resistance. An equivalent simplified circuit needs to be extracted in order to apply the well-known formula for the cutoff frequency of the diode, $f_c = 1/(2\pi R_s C_j)$, defined as the frequency where the power that falls in the junction resistance is halved[39]. Thus, if the equivalent series resistance is approximated to $R_{s,eq} = R_s + R_2$, then f_c equals to 0.207 GHz and 0.45 GHz for the TIM and TM diodes, respectively. However, due to the impact of C_2, which progressively reduces the impact of R_2, the total capacitance reduces to $C_T = (C_1//C_2)$, where the operator "//" refers to the parallel or series combination of the resistors or capacitors, respectively. The extracted f_c equals then around 0.5 GHz for the diode with sputtered oxide and 1.3 GHz for the one without oxide. It is to be expected that the cutoff frequency of these diodes lies between these two values. Nevertheless, it is important to highlight that this FOM, although practical for the sake of comparison against other incumbent technologies, fails to accurately evaluate the real performance of the devices when employed in circuits, as it will be later discussed. Furthermore, as it will be shown, it describes the limits of the device in applications that rely on the nonlinearity of the junction resistance but does not provide information about further applications based on other nonlinearities, e. g. the tunable capacitances that, indeed, can lead to nonlinear applications operating beyond the defined junction-resistance-related cutoff frequency, as will be shown.

RF applications

The employment of diodes in RF applications has been extensively studied in various applications[32,40]. The operating principle exploits the nonlinear current/voltage characteristics of these devices, which can be approximated by the Taylor expansion as:

$$I(v) = I_0 + v\frac{dI}{dV}\bigg|_{V_0} + \frac{1}{2}v^2\frac{d^2I}{d^2V}\bigg|_{V_0} + \ldots, \tag{8}$$

where $I_0 = I(V_0)$ and V_0 is the bias voltage. When a small-signal voltage with a fundamental frequency, f_0, is applied to (8), due to the terms with orders higher than 1, apart from the original signal, several harmonics and a DC component are generated. Moreover, when more than one signal is applied, these harmonics lead to mixing products in the form of frequency components equal to the sum and difference of these harmonics. By this means, several applications can be pursued depending on the desired output frequency. Furthermore, in the particular case of mixers or frequency converters where a large pump signal is needed, other effects coming from the large-signal effects and variable capacitances have been recently reported[41]. In the following, two RF nonlinear applications are tested to prove the potential of the proposed devices. In addition to the individual description of the results, the photographs of the built setups are included in Supplementary Fig. 9.

Firstly, the mixer setup shown in Fig. 5a is built as described in Methods. The performance of the TIM-based mixer acting as an upconverter is shown in Fig. 5b for an 8-dBm input local oscillator (LO) signal at 2.5 GHz and 5 GHz, and a 100-MHz and -16-dBm intermediate frequency (IF) signal. Besides, Fig. 5c shows the spectrum measured for a TIM-based downconverter for an input LO signal of 8 dBm at 2.5 GHz and an RF signal at 2.8 GHz and -16 dBm. The achieved conversion gain for the upconverted RF signals are -24 dB and -29 dB, respectively, and -39 dB for the downconverter operation. It should be highlighted that the difference in these results is to a greater extent due to the proper setup, and not the intrinsic characteristics of the device itself. Then, as reflected in Fig. 5d, the devices are tested for upconversion at even higher frequencies. The measurements prove that the TIM diode provides useful nonlinearity also at frequencies way beyond its predicted f_c. Furthermore, the device is biased at -1.5 V, where the diode is far from its most nonlinear region lying around 0.6 V, as can be noticed from Supplementary Fig. 6. This proves that the nonlinear performance relies not only on the nonlinear junction resistance but also on the junction capacitance and the proper series resistance. As can be noticed from the measurement results, a high number of harmonics and mixing frequencies appear at the output. Therefore, an improvement in the conversion gain performance can be achieved by introducing an output matching network, filtering the unwanted signals, and better port isolation. Nevertheless, for the purpose of this work, it is precisely these results that prove the excellent nonlinear behavior of TIM devices and demonstrate their suitability for future RF applications. Further analysis of the performance over input power can be found in Supplementary Fig. 10.

The next considered application is an RF power detector, the measurement setup, as well as its schematics, are shown in Fig. 6a, b, respectively. Power detectors are crucial components in several RF applications, including AM demodulators, six-port receivers, and automatic gain control systems[42,43]. In addition, for such applications, devices that conduct at zero bias, *i. e* that do not require an additional voltage source, are of special interest since they would facilitate the implementation of wireless, low-power, and wearable circuits. However, as already discussed, it is observed that the nonlinearity of the diode with sputtered TiO_2 is maximum at around 0.6 V. Additionally, the current around 0 V in the TIM-device, due to the analyzed sizeable barrier (see Fig. 3) and corresponding observed high asymmetry (Supplementary Fig. 6) is in the range of nano-amperes. Both factors determine the performance of this device as a zero-bias power detector. Thus, although around 0 V a predicted responsivity for the TIM device of around 3 $A \cdot W^{-1}$ can be reached (see Supplementary Fig. 6), at this bias point the current levels are too low in order to be detected even if a high impedance (e. g., a 1-MΩ load) is employed. On the contrary, TM-diodes (without oxide layer) show a higher current density (see Fig. 3) and a lower asymmetry (see Supplementary Fig. 7) that make them excellent candidates for building zero-bias power detectors. The performance of the TM-based detector in terms of output DC voltage vs. input RF power and tangential responsivity vs. frequency is shown in Fig. 6c, d, respectively. The achieved linear-in-dB dynamic range (DR) reaches over 40 dB, while the responsivity at -20 dBm at 1 GHz achieves 257 $V \cdot W^{-1}$. Beyond this frequency, the responsivity decreases to around 50 $V \cdot W^{-1}$ at 2.5 GHz, 25 $V \cdot W^{-1}$ at 5 GHz, and values ranging around 10 $V \cdot W^{-1}$ beyond 20 GHz (see Fig. 6d). This behavior is also constrained by the external components introduced by the measurement setup, where the input matching is actually not regular over the whole bandwidth. Yet, the measured responsivity is observed to be reduced from around 1.2 GHz, in agreement with the previously predicted cutoff frequency. As expected, contrarily to the TIM-based mixer, the role of the nonlinear resistor, R_1, is decisive for the conduct of the

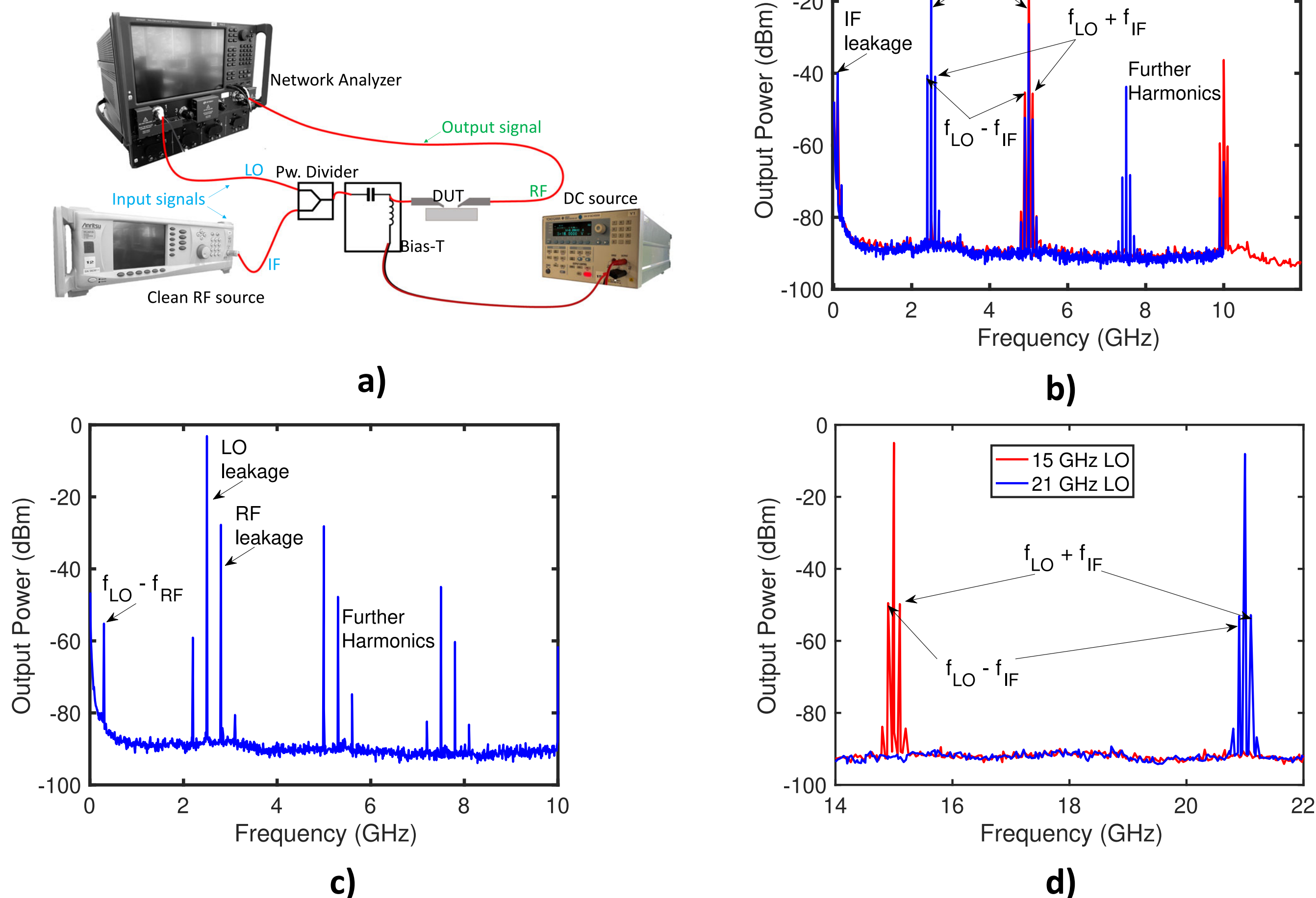

Fig. 5 TIM-based mixer results under a -1.5 V bias voltage. a Measurement setup. **b** Output spectrum for the upconverter tested for 2.5 GHz and 5 GHz LO signals ($P_{LO} = 8$ dBm) for an intermediate frequency signal of $f_{IF} = 100$ MHz and $P_{IF} = -16$ dBm. **c** Output spectrum of the mixer under downconverter operation ($f_{RF} = 2.8$ GHz and $P_{RF} = -16$ dBm; $f_{LO} = 2.5$ GHz and $P_{LO} = 8$ dBm). **d** Output spectrum for the upconverter mixer for a local oscillator with frequency 15 GHz ($P_{LO} = 8$ dBm) and 21 GHz ($P_{LO} = 8$ dBm), showing the potential capabilities of TIM diodes to perform at this frequency range. The cable losses are not de-embedded.

detector, thus, the results are limited by the f_c of the diode[44]. As already mentioned, in both applications the external components inevitably interfere with the performance and a full on-chip implementation of the circuits would lead to further improvement of the results.

DISCUSSION

The relevance of diodes as RF components is crucial and has been investigated since the advent of communication electronics. The search for suitable devices capable of RF detection and frequency conversion has been widely analysed[40], and recently, thin-film devices based on emerging technologies have been reported. These include MoS_2[4,44], ZnO[45], graphene[3], and IGZO[46] among others, to implement mainly either metal-insulator-metal (MIM) or Schottky diodes. In regards to the former type and its variants, which include MIM structures and devices with graphene instead of the cathode metal, the investigation has been carried out on what factors impact the nonlinearity and responsivity performance[33]. The choice of the metals together with the thickness of the oxide affects the results, and it has been proven that there is a trade-off between the achieved asymmetry and the reached ON currents[31]. As already discussed, this effect is also present in this work, where the TM-diode presents a behavior similar to the one reported in[47] for different MIM diodes. The TM diode achieves higher current densities at zero bias at the expense of its asymmetry. These types of devices resemble the reported bilateral nonlinear resistors in[48], which were employed as detectors and presented several advantages in terms of high signal-to-noise ratios at low input powers precisely due to their symmetry. The possibility of implementing either TM or TIM diodes proves the versatility of the material in regard to the feasable implementation of different heterostructures that according to their characteristics can target different applications.

In regards to the direct comparison of the performance among diodes, it needs to be done carefully since different setups and applications might play a big role in the obtained results. For instance, the work in[39] based on a vertical WSe_2 diode demonstrates a detector with an input signal with a constant amplitude of 1 V for a 50-Ω input resistance (10 dBm input power). The detected voltages, for a diode with 70 μm^2 junction area, are around 0.8 V, similar to the reported values in this work for frequencies below f_c, whereas the current density is over one order of magnitude higher in the Te-based diode (at 1 V). In regards to the achieved cutoff frequencies the work in[39] reports a discrepancy between the theoretical (intrinsic) cutoff frequency and that shown for the detector (extrinsic), which goes up to 10 GHz but is three times lower than the former. This is a direct

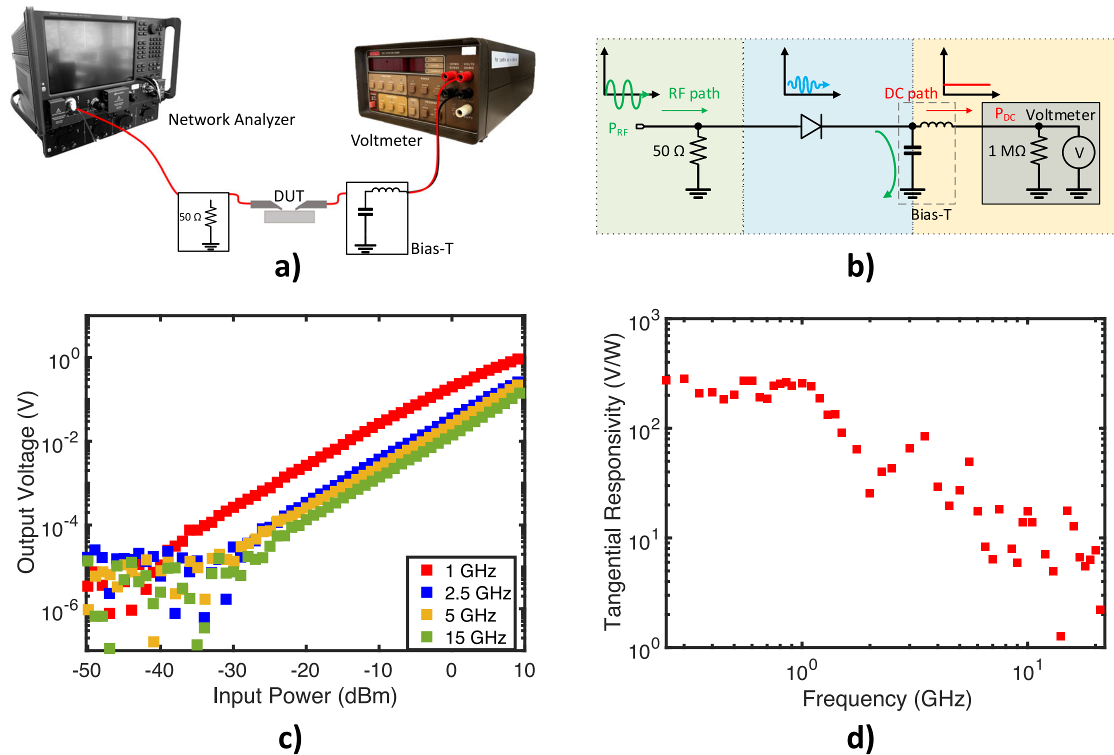

Fig. 6 Power detection measurement results. a Power detector measurement setup. The 50-Ω resistor serves as the input matching network and the output bias tee as a low-pass filter and RF return path. **b** Schematic of the implemented detector. **c** Output DC voltage over RF input power for the TM diode. **d** Tangential responsivity of TM two-terminal device at -20 dBm over frequency.

consequence of calculating the intrinsic value from only the extracted small-signal junction capacitance and resistance and is avoided in our work by considering all the elements of the diode. Likewise, this is addressed in[45], which also highlights the dependence of the extrinsic cutoff frequency with the input power (large-signal behavior), in this case, based on lateral ZnO diodes with different widths (*W*). As[39], the cited work reports up to one order of magnitude less for the extrinsic cutoff frequency, which still reaches up to 6 GHz and 3.6 GHz for their smallest ($W = 500\mu m$) and largest ($W = 5 mm$) device, respectively. However, in[45] the reported output voltage for a 5-dBm input signal equals 0.09 V (smallest device) and 0.2 V (largest device), while this work achieves 0.5 V within the 3-dB bandwidth. It should be noticed that both[39] and[45] report relatively large devices compared to the Te-based diode, where the latter also observes a trade-off between the size and achieved detected voltages. It is the high current density of the TM diode that despite its smaller size allows a comparable performance for the measured detector, while further analysis is still needed to study the impact of scaling the device on the cutoff frequency. Furthermore, the potential of the TM diode is clearly demonstrated by the excellent achieved tangential responsivity at -20 dBm and the minimum detected power that, within the bandwidth of the diode, is comparable to that of CMOS-based technologies[49], while being zero-biased. Moreover, the achieved superior dynamic range is comparable to that in graphene-based diodes[50], while having the advantage of being environmentally stable conversely to the graphene case.

Regarding diode-based mixers, a highly nonlinear device is crucial, but the measurement setup and the circuit topology play a big role in the achieved performance. When considering only hybrid circuits (i. e, where the device is on-chip and the rest of the elements are connected externally) on rigid substrates and based on single devices, two works can be compared. Firstly, in[37], a mixer based on a graphene diode is reported. While the input setup is similar to the one used in this work, at the output an IF buffer is used, which allows the diode to drive the 50-Ω load provided by the measurement equipment and matches the output impedance of the diode. The results show a conversion loss as low as 15 dB at 2.4 GHz. In our work, the potential of the device is evaluated, hence, the delivered input power is maximized with a proper matching while the output lacks any sort of filtering. As previously discussed, the apparition of a high number of harmonics reflects how nonlinear the device is, even beyond the cutoff frequency. Therefore, for the stated purpose and because the TIM diode is capable of being attached directly to a 50-Ω load, which is also a direct consequence of the high current density and nonlinearity achieved by the device, a buffer was not included and the conversion loss is 24 dB at 2.4 GHz. Then, the work in[51], shows the results based on a MoS_2 FET. The setup is analogue to the one employed in this work but reaches a conversion gain of around 10 dB lower at 1.5 GHz than the gain achieved by the TIM-diode at 2.5 GHz for similar IF and LO powers.

Finally, it should be noted that the state-of-the-art diodes based on bulk semiconductors show excellent performance way beyond the cutoff frequency of the proposed diodes and beyond the mixer frequencies reported in this work. Yet, besides, for instance, being constrained in terms of dynamic range in the case of the power detectors, the major drawback of bulk semiconductors is that they lack the possibility of targeting emerging flexible technologies. Consequently, the focus of this discussion has been the comparison with those 2D materials that are in a higher technology readiness level. In this regard, comparable behaviour and even the outstanding performance of the Te-based diodes has been demonstrated. Nevertheless, it is important to highlight that intensive study of wafer-scale processing methods is still fundamental and is being carried out, as recently reported in the literature[52,53]. This is essential to further improve and develop devices as well as to realize statistical analysis of the performance and reliability of the processes. Ultimately, this will define the prosperity of the material beyond research.

This work proposes and analyses the electrical performance of two-dimensional Te when used in an MIS and an MS diode structure. The fabrication and charge transport mechanisms are described in detail for the two structures showing the impact of the insulator layer in the current behaviour. Then, each type of diode is fully characterized in the DC and RF domain in order to evaluate the potential applications and their limitations. Moreover, small-signal equivalent circuits of the devices are extracted and two RF applications suitable for each of the diodes, TIM and TM, have been demonstrated. Both, power detectors and mixers are key blocks in transceiver front-ends, hence, the research on the applicability of 2D materials to RF systems is thriving. Beyond the extraction of traditional FOMs, it is shown that devices need to be tested in real circuit implementations to fully exploit their properties. In this manner, a zero-bias power detector based on the nonlinear resistance of the diode is presented, but also a reversed-biased mixer demonstrates the possibilities of using different nonlinearities of the diode beyond their theoretical f_c. The presented work and applications demonstrate the flexibility of the introduced diode structures that could be optimized according to the target application. This is the first time RF applications are shown for any 2D Te-based device, and the results show a promising performance despite the infant stage of the technology. It is the belief of the authors that this is a first step towards demonstrating the wide possibilities of 2D Te for future RF applications.

METHODS

Synthesis of the 2D Te

The 2D Te flakes are prepared following a standard hydrothermal synthesis procedure. Firstly, 0.09 g of Na_2TeO_3 and 0.5 g of PVP-58K are added to 33 ml of de-ionized (DI) water under magnetic stirring to form a homogeneous solution. Next, 3.33 ml of aqueous ammonia (25% wt/wt %) is added followed by 1.67 ml of hydrazine hydrate (85% wt/wt %). The mixture is sealed in a 50 ml Teflon-lined stainless steel autoclave and heated at 180 °C for 20 hours before naturally cooling it down to room temperature. For purification, the obtained silver-grey product is washed several times by centrifugation at 5000 rpm for 5 minutes to remove the remaining PVP. After washing and purification, the Te flakes are re-dispersed in DI water. The obtained flakes reach a typical total thickness of 160 nm, as shown in Supplementary Fig. 3.

Te flake characterization measurement

The thickness of the Te flake was measured by atomic force microscopy (AFM, Bruker icon). The Raman spectra of samples were obtained using a Renishaw via confocal Raman microscope equipped with a 514 nm continuous-wave excitation laser. The TEM lift-out sample was prepared with an FEI (now part of Thermo Fisher) Helios NanoLab 650 FIB/SEM system, using 30 keV Ga ion beams for lifting out and thinning and 16 kV Ga ion beams for final polishing. The SAED, HR-TEM, HAADF STEM, and EDX images were taken with an FEI (Thermo Fisher) Tecnai Osiris S/TEM system equipped with Bruker SuperX EDX detectors and operated at 200 keV.

DC characterization

The TIM diode was characterised in DC by means of the 4156B Agilent Semiconductor Parameter Analyzer connected to a probe station. The measurements were carried out from -1.5 to 1.5 V in 3 mV. Higher voltages are not applied in order to protect both, the Te flake and the oxide due to the high current density of the devices. The TM diode was measured by means of a Keithley 4200-SCS semiconductor characterization system also connected to a probe station. The measurements were carried out from -1 V to 1 V in 10 mV intervals. The current was limited to 100 μA in order to protect the device. Both diodes were measured at room temperature.

S-parameter measurements and equivalent circuit

The two-port *S*-parameter measurements were performed by a network analyzer (NA) PNA-X © Keysight. Prior to carrying out the measurements, an on-wafer calibration substrate kit (Form Factor GSG 100 μm pitch 101-190) is used with the commercial short-open-load-through (SOLT) structures to de-embed the probes and cables of the setup. The frequency sweep covered from 100 MHz to 67 GHz under different bias voltages ranging from -1.5 V to 1.5 V in 0.15 V steps. The extracted small-signal model is extracted for an applied voltage of 0 V. The validity of the model is confirmed when comparing simulation and measurement results under the studied frequency range. The parameters were extracted and simulated by means of the Advanced Design Software (ADS) from Keysight. In order to extract the value of the different parameters, the typical Schottky diode is employed as an starting point. Assuming that the pad parasitics are negligible at lower frequencies, the one-port input impedance is extracted as $Z_{in} = 1/Y_{11}$, where Y_{11} is obtained from transforming the S-parameters into the equivalent two-port Y-parameters[32]. The junction resistance at the bias point of interest is obtained as the inverse of the first derivative $\frac{dI}{dV}|_{V_0}$. The series resistance, on the other hand, is the dominant resistance when $f >> f_c$, thus, this value is firstly approximated from the real part of Z_{in} at the maximum measured frequency. The junction capacitance can be obtained as $C_j = imag(Y_{11})/(2\pi f)$, which is observed to be frequency-dependent. Therefore, additional capacitors need to be considered and the junction capacitance can be initially approximated by the value of $C_1 = C_j(f_{min})$ where f_{min} is the minimum measured frequency (10 MHz). Further RC blocks can be obtained when considering the extracted 1-port impedance as a transfer function V_{out}/I_{in} that follows the Bode diagram approximations for each pole and zero. At higher frequencies the impact of the pads can be observed and the values extracted if the device is considered as an equivalent π-network[32] (page 194). Finally, the value optimization can be carried out in ADS to fit the required frequency range.

Mixer characterization

The mixer characterization was performed with the network analyzer (NA) PNA-X © Keysight as the LO source and the RF port, and the Anritsu MG3691B RF CW Signal Generator was used as IF source. The biasing was provided by an external bias tee at the input LO/IF port (anode) and the internal one of the NA at the RF port (cathode). An external wideband (up to 26 GHz) 6-dB power divider was employed to split the LO and IF paths at the input. This block naturally acts as the input matching network, but provides low isolation (6 dB) between the ports. At the output no matching network was included. Consequently, in the spectrum recorded at the output the LO leakage and higher harmonics are present.

Power detector characterization

The power detector measurements were carried out with the network analyzer (NA) PNA-X © Keysight as RF source, and the Keithley 617 Programmable Electrometer as the voltmeter. The latter is connected through a bias tee that acts as a low-pass filter, and a shunted-to-ground 50 Ω connected at the input is used to achieve the required input impedance matching. Since the matching is resistive and externally connected, it is observed that the return loss is not regular over frequency. The full integration of chip and another type of matching network would lead to improved results. Then, the power level of the NA is calibrated by

the power sensor U8498A from Keysight. The power is swept from -50 to 5 dBm and so is the frequency from 0.1 GHz up to 21 GHz. Further frequencies are not considered since the bias tee is valid up to 18 GHz, i. e. the setup itself would limit the performance.

DATA AVAILABILITY

The data that support the findings of this study are available from the corresponding author upon reasonable request.

CODE AVAILABILITY

The code that supports the findings of this study are available from the corresponding author upon reasonable request.

Received: 3 June 2023; Accepted: 12 September 2023;
Published online: 27 September 2023

REFERENCES

1. Novoselov, K. S. et al. Electric field effect in atomically thin carbon films. *Science* **306**, 666–669 (2004).
2. Saeed, M. et al. Graphene-based microwave circuits: a review. *Adv. Mater.* **34**, 2108473 (2022).
3. Shaygan, M. et al. High performance metal–insulator–graphene diodes for radio frequency power detection application. *Nanoscale* **9**, 11944–11950 (2017).
4. Askar, A. M., Saeed, M., Hamed, A., Negra, R. & Adachi, M. M. Thickness-modulated lateral MoS 2 diodes with sub-terahertz cutoff frequency. *Nanoscale* **13**, 8940–8947 (2021).
5. Xiong, Y. et al. P-Type 2D Semiconductors for Future Electronics. *Adv. Mater.* 2206939 (2022).
6. Shi, Z. et al. Two-dimensional tellurium: Progress, challenges, and prospects. *Nano-Micro Lett.* **12**, 1–34 (2020).
7. Zhu, Z. et al. Multivalency-Driven Formation of Te-Based Monolayer Materials: A Combined First-Principles and Experimental study. *Phys. Rev. Lett.* **119**, 106101 (2017).
8. Reed, E. J. Two-dimensional tellurium. *Nature* **552**, 1–2 (2017).
9. Zhao, C. et al. Evaporated tellurium thin films for p-type field-effect transistors and circuits. *Nat. Nanotechnol*. 1–6 (2019).
10. Zhao, C. et al. Tellurium Single-Crystal Arrays by Low-Temperature Evaporation and Crystallization. *Adv. Mater*. 2100860 (2021).
11. Guo, J. et al. Two-dimensional tellurium–polymer membrane for ultrafast photonics. *Nanoscale* **11**, 6235–6242 (2019).
12. Wang, Y. et al. Field-effect transistors made from solution-grown two-dimensional tellurene. *Nat. Electron.* **1**, 228–236 (2018).
13. Castellanos-Gomez, A. et al. Deterministic transfer of two-dimensional materials by all-dry viscoelastic stamping. *2D Mater.* **1**, 011002 (2014).
14. Rivera, B., Baker, R. J. & Melngailis, J. Design and layout of Schottky diodes in a standard CMOS process. In *2001 International Semiconductor Device Research Symposium. Symposium Proceedings*, 79–82 (IEEE, 2001).
15. Chaves, F. A. et al. A physics-based model of gate-tunable metal-graphene contact resistance benchmarked against experimental data. *2D Mater.* **2**, 025006 (2015).
16. Ma, N. & Jena, D. Carrier statistics and quantum capacitance effects on mobility extraction in two-dimensional crystal semiconductor field-effect transistors. *2D Mater.* **2**, 015003 (2015).
17. Şahin, C., Rou, J., Ma, J. & Pesin, D. A. Pancharatnam-Berry phase and kinetic magnetoelectric effect in trigonal tellurium. *Phys. Rev. B* **97**, 205206 (2018).
18. Enderlein, R. & Hache, A. Valence and Conduction Band Structure and Infrared Optical Properties of Tellurium in the Presence of Pressure. *Phys. Status Solidi B* **60**, 739–749 (1973).
19. Kormányos, A. et al. k.p theory for two-dimensional transition metal dichalcogenide semiconductors. *2D Mater.* **2**, 022001 (2015).
20. Rasmussen, F. A. & Thygesen, K. S. Computational 2D Materials Database: Electronic Structure of Transition-Metal Dichalcogenides and Oxides. *J. Phys. Chem. C* **119**, 13169–13183 (2015).
21. Allain, A., Kang, J., Banerjee, K. & Kis, A. Electrical contacts to two-dimensional semiconductors. *Nature Mater.* **14**, 1195–1205 (2015).
22. Anwar, A., Nabet, B., Culp, J. & Castro, F. Effects of electron confinement on thermionic emission current in a modulation doped heterostructure. *J. Appl. Phys.* **85**, 2663–2666 (1999).
23. Ang, Y. S., Yang, H. Y. & Ang, L. K. Universal Scaling Laws in Schottky Heterostructures Based on Two-Dimensional Materials. *Phys. Rev. Lett.* **121**, 56802 (2018).
24. Ang, Y. S., Cao, L. & Ang, L. K. Physics of electron emission and injection in two-dimensional materials: Theory and simulation. *InfoMat* **3**, 502–535 (2021).
25. Taur, Yuan and Ning, T. H. *Fundamentals of Modern VLSI Devices*, 2nd Edition (Cambridge Univ. Press, New York, 2005).
26. Crowell, C. & Rideout, V. Normalized thermionic-field (T-F) emission in metal-semiconductor (Schottky) barriers. *Solid State Electron. Lett.* **12**, 89–105 (1969).
27. Padovani, F. A. & Stratton, R. Experimental Energy-Momentum Relationship Determination Using Schottky Barriers. *Phys. Rev. Lett.* **16**, 1202–1204 (1966).
28. Simmons, J. G. Generalized Formula for the Electric Tunnel Effect between Similar Electrodes Separated by a Thin Insulating Film. *J. Appl. Phys.* **34**, 1793–1803 (1963).
29. Simmons, J. G. Potential barriers and emission-limited current flow between closely spaced parallel metal electrodes. *J. Appl. Phys.* **35**, 2472–2481 (1964).
30. Pasadas, F. et al. Large-Signal Model of the Metal-Insulator-Graphene Diode Targeting RF Applications. *IEEE Electron Device Lett.* **40**, 1005–1008 (2019).
31. Urcuyo, R., Duong, D. L., Jeong, H. Y., Burghard, M. & Kern, K. High Performance Graphene–Oxide–Metal Diode through Bias-Induced Barrier Height Modulation. *Adv. Electron. Mater.* **2**, 1600223 (2016).
32. Pozar, D. *Microwave Engineering, 4th Edition* (Wiley, 2011).
33. Periasamy, P. et al. Metal–insulator–metal diodes: Role of the insulator layer on the rectification performance. *Adv. Mater.* **25**, 1301–1308 (2013).
34. Lipka, K.-M., Splingart, B., Erben, U. & Kohn, E. LT-GaAs-MIS-diode characteristics and equivalent circuit model. In *Proceedings of IEEE/Cornell Conference on Advanced Concepts in High Speed Semiconductor Devices and Circuits*, 103–110 (IEEE, 1993).
35. Katsube, T., Adachi, Y. & Ikoma, T. Small Signal Equivalent Circuit for an MIS Tunnel Diode. *Jpn. J. Appl. Phys.* **13**, 504 (1974).
36. Zhang, A. & Gao, J. Comprehensive analysis of linear and nonlinear equivalent circuit model for GaAs-PIN diode. *IEEE Trans. Ind. Electron.* **69**, 11541–11548 (2021).
37. Saeed, M. et al. Metal–insulator–graphene diode mixer based on CVD graphene-on-glass. *IEEE Electron Device Lett.* **39**, 1104–1107 (2018).
38. Hemour, S. et al. Towards Low-Power High-Efficiency RF and Microwave Energy Harvesting. *IEEE Trans. Microw. Theory Tech.* **62**, 965–976 (2014).
39. Yang, S. J. et al. Ultrafast 27 GHz cutoff frequency in vertical WSe2 Schottky diodes with extremely low contact resistance. *Nat. Commun.* **11**, 1–9 (2020).
40. Torrey, H. C. & Whitmer, C. A.*Crystal rectifiers*, vol. 15 (McGraw-Hill Book Company, 1948).
41. Palacios, P., Saeed, M. & Negra, R. Design Considerations for a Low-Power Fully Integrated MMIC Parametric Upconverter in SiGe BiCMOS. *IEEE J. Solid-State Circuits* 1–16 (2023).
42. Qayyum, S. & Negra, R. 0.16 mW, 7–70 GHz distributed power detector with 75 dB voltage sensitivity in 130 nm standard CMOS technology. In *2017 12th EuMIC*, 13–16 (IEEE, 2017).
43. Saeed, M. et al. Graphene integrated circuits: new prospects towards receiver realisation. *Nanoscale* **10**, 93–99 (2018).
44. Zhang, X. et al. Two-dimensional MoS2-enabled flexible rectenna for Wi-Fi-band wireless energy harvesting. *Nature* 1 (2019).
45. Georgiadou, D. G. et al. 100 GHz zinc oxide Schottky diodes processed from solution on a wafer scale. *Nat. Electron.* **3**, 718–725 (2020).
46. Loganathan, K. et al. Rapid and up-scalable manufacturing of gigahertz nanogap diodes. *Nat. Commun.* **13**, 3260 (2022).
47. Alshehri, A. H. et al. Metal-Insulator-Insulator-Metal Diodes with Responsivities Greater Than 30 A W-1 Based on Nitrogen-Doped TiOx and AlOx Insulator Layers. *Adv. Electron. Mater.* **7**, 2100467 (2021).
48. Bridges, J. E. Pseudo-Rectification and Detection by Simple Bilateral Nonlinear Resistors. *Proc. IRE* **49**, 469–478 (1961).
49. Qayyum, S. & Negra, R. Analysis and Design of Distributed Power Detectors. *IEEE Trans. Microw. Theory Tech.* **66**, 4191–4203 (2018).
50. Saeed, M. et al. Zero-Bias 50-dB Dynamic Range Linear-in-dB V-Band Power Detector Based on CVD Graphene Diode on Glass. *IEEE Trans. Microw. Theory Tech.* **66**, 2018–2024 (2018).
51. Gao, Q. et al. Scalable high performance radio frequency electronics based on large domain bilayer MoS2. *Nat. Commun.* **9**, 4778 (2018).
52. Kim, T. et al. Growth of high-quality semiconducting tellurium films for high-performance p-channel field-effect transistors with wafer-scale uniformity. *NPJ 2D Mater. Appl.* **6**, 4 (2022).
53. Kim, C. et al. Atomic Layer Deposition Route to Scalable, Electronic-Grade van der Waals Te Thin Films. *ACS Nano* (2023).
54. Sang, D. K. et al. Electronic and optical properties of two-dimensional tellurene: from first-principles calculations. *Nanomater.* **9**, 1075 (2019).

55. Qiao, J. et al. Few-layer Tellurium: one-dimensional-like layered elementary semiconductor with striking physical properties. *Science bulletin* **63**, 159–168 (2018).
56. Anzin, V., Eremets, M., Kosichkin, Y. V., Nadezhdinskii, A. & Shirokov, A. Measurement of the energy gap in tellurium under pressure. *Phys. Status Solidi A* **42**, 385–390 (1977).
57. Yang, D.-Q. et al. Band Structure and Lattice Vibration of Elemental Tellurium Investigated by Temperature-Dependent Mid-and-Far Infrared Transmission and Raman Spectroscopy. *Phys. Status Solidi B* **259**, 2100625 (2022).
58. Shinno, H., Yoshizaki, R., Tanaka, S., Doi, T. & Kamimura, H. Conduction band structure of tellurium. *J. Phys. Soc. Jpn.* **35**, 525–533 (1973).
59. Thanh, D. Effective mass approximation for acceptors in tellurium. *Solid State Commun.* **9**, 631–634 (1971).
60. Jałochowski, M., Mikołajczak, P. & Subotowicz, M. Measurements of the work function and the fermi level in thin tellurium films. *Phys. Status Solidi A* **14**, K135–K137 (1972).
61. Caldwell, R. S. & Fan, H. Optical properties of tellurium and selenium. *Phys. Rev. Appl.* **114**, 664 (1959).
62. De Vos, A. & Van Dhelsen, D. The temperature dependence of the electrical properties of thin tellurium films. *Rev. Phys. Appl.* **14**, 815–820 (1979).

ACKNOWLEDGEMENTS

This work is part of the research project TED2021-129769B-I00 "FlexPowHar" funded by MCIN/AEI/10.13039/501100011033 and the European Union NextGenerationEU/PRTR. Adittionally, the authors acknowledge German Research Foundation (DFG) under the projects GLECS2 (No. 653408), MOSTFLEX (653414), the Natural Sciences and Engineering Research Council (NSERC) (RGPIN-2017-05810 and ALLRP 577611-22), the European Commission under the Horizon 2020 projects Graphene Flagship (No. 785219 and 881603), PAIDI 2020 and European Social Fund Operational Programme 2014-2020 no. 20804, and from the Ministerio de Universidades, José Castillejo grant no. CAS21/00483. A.M.A. is supported by a Vanier Canada Graduate Scholarship. We would like to acknowledge CMC Microsystems for the provision of products and services that facilitated this research. This work made use of the 4DLABS shared facilities supported by the Canada Foundation for Innovation (CFI), British Columbia Knowledge Development Fund (BCKDF), and Western Economic Diversification Canada (WD). This work was further supported by Simon Fraser University.

AUTHOR CONTRIBUTIONS

A.A., P.P. and F.P. contributed equally to this work. A.A., P.P., F.P., M.S., R.N. and M.A. conceived the design of the diodes. A.A. fabricated both type of devices and characterized the fabrication process. M.R.M. performed the Raman characterization. A.A. and P.P. characterized the devices in DC. F.P. developed the theoretical analysis and electrostatic model. P.P. characterized the devices in RF and extracted the equivalent circuit. P.P., M.S. and R.N. conceived the suitable applications and their setups. P.P. carried out the application measurements and data analysis. All the authors contributed to interpreting the data and writing the manuscript.

FUNDING

Open Access funding enabled and organized by Projekt DEAL.

COMPETING INTERESTS

The authors declare no competing interests.

ADDITIONAL INFORMATION

Supplementary information The online version contains supplementary material available at https://doi.org/10.1038/s41699-023-00433-w.

Correspondence and requests for materials should be addressed to Abdelrahman M. Askar, Paula Palacios or Francisco Pasadas.

Reprints and permission information is available at http://www.nature.com/reprints

Publisher's note Springer Nature remains neutral with regard to jurisdictional claims in published maps and institutional affiliations.

Open Access This article is licensed under a Creative Commons Attribution 4.0 International License, which permits use, sharing, adaptation, distribution and reproduction in any medium or format, as long as you give appropriate credit to the original author(s) and the source, provide a link to the Creative Commons license, and indicate if changes were made. The images or other third party material in this article are included in the article's Creative Commons license, unless indicated otherwise in a credit line to the material. If material is not included in the article's Creative Commons license and your intended use is not permitted by statutory regulation or exceeds the permitted use, you will need to obtain permission directly from the copyright holder. To view a copy of this license, visit http://creativecommons.org/licenses/by/4.0/.

© The Author(s) 2023